ABSTRACT

SPECTRAL 3D RECONSTRUCTION
BASED ON MACROSCOPIC OCT IMAGING

by
Xingyu Zhou

Various optical technologies have been utilized to improve art conservation by art conservators, such as laser triangulation, stereophotogrammetry, structured light, laser scanner and time of flight sensors. These methods have been deployed to capture the 3D or surface topography information of sculptures and architectures. Optical coherence tomography (OCT) has introduced new imaging methods to study the surface features and subsurface structures of delicate cultural heritage objects. However, despite its higher spatial resolution, the field of view (FOV) of OCT severely limits the size of the scanning area and does not allow macroscopic examination. To solve this issue, we develop and validate a hybrid scanning platform combined with effective algorithm for real-time sampling and artifact removal to achieve macroscopic OCT (macro-OCT) imaging and generate the spectral 3D reconstruction of impressionist style oil paintings as a digital model.

SPECTRAL 3D RECONSTRUCTION
BASED ON MACROSCOPIC OCT IMAGING

by
Xingyu Zhou

A Thesis
Submitted to the Faculty of
New Jersey Institute of Technology
In Partial Fulfillment of the Requirements for the Degree of
Master of Science in Electrical Engineering

Helen and John C. Hartmann Department of
Electrical and Computer Engineering

May 2020

APROVAL PAGE

SPECTRAL 3D RECONSTRUCTION
BASED ON MACROSCOPIC OCT IMAGING

Xingyu Zhou

Dr. Xuan Liu, Thesis Advisor   Date
Associate Professor of Electrical and Computer Engineering, NJIT

Dr. Haim Grebel, Committee Member   Date
Professor of Electrical and Computer Engineering, NJIT

Dr. Yi Yang, Committee Member   Date
Associate Professor of Engineering, Penn State

BIOGRAPHICAL SKETCH

Author: Xingyu Zhou

Degree: Master of Science

Date: May 2020

Undergraduate and Graduate Education:

- Master of Science in Electrical Engineering,
  New Jersey Institute of Technology, Newark, NJ, 2020

- Bachelor of Engineering in Microelectronics Science&Engineering,
  Jiangnan University, Jiangsu, P. R. China, 2017

Major: Electrical Engineering

TABLE OF CONTENTS

TABLE OF CONTENTS
(Continued)

Chapter   **Page**

LIST OF FIGURES

CHAPTER 1

INTRODUCTION

1.1 Objective

The objective of this thesis is to develop 3D reconstruction capability based on macroscopic OCT imaging with a large field of view (FOV) for oil paintings. The OCT images provide the surface and subsurface information that can be used to construct the digital model of the artwork in computer.

To protect and examine heritage works, art conservators need to determine the state of the art works. Many technologies have been applied to this area to improve the conservation efforts [1][2]. OCT as a non-invasive imaging method is used in art conservation area to find tiny texture or feather on the surface of the objects [3][4][5]. The high resolution of OCT allows the researchers to examine detailed structural features of the art works [6]. However, OCT has a limited field of view. It remains challenging for researchers to have a macro understanding for the whole painting or sculpture in 3D according to the information presented by OCT images. Therefore, it is necessary to develop an OCT system with a large field of view and improve the presentation of OCT data. The thesis is organized as the follows. First, the imaging platform and data acquisition method is introduced. Afterwards, the spectral 3D reconstruction of an impressionist style oil painting with our stitching algorithm is demonstrated.

1.2 Background Information

Laser triangulation, stereophotogrammetry, structured light, laser scanner and time of flight sensors have been used to capture the 3D information of sculptures and architectures. Other devices with 3D scanning function have also been used in art conservation efforts. For example, 3D data collected based on conoscopic micro-profilometry/holography [7][8][9] has been integrated with 2D data to improve the conservation strategy [10][11]. A 3D range camera based on optical triangulation with fringe pattern projection was used to capture the 3D surface profile of "Adorazione dei Magi" by Da Vinci for conservation monitoring [12]. A high-resolution color laser scanner based on trigonometry was used to scan the famous painting Mona Lisa and then generated the 3D coordinates, while simultaneously capturing the spectral information of the object [13]. More recent research has applied terahertz reflectometry to generate the surface profile and the cross-sectional information of paintings [14][15], which enables conservators to evaluate the layer structure of paintings. Other methods such as x-ray or CT computer tomography and magnetic resonance imaging have been applied to acquire cross-sectional images and detect the 3D structure of the object. These methods allow macroscopic characterization. However, they lack the spatial resolution for microscopic examinations [16][17].

The unique features of optical coherence tomography (OCT) have brought this imaging methods to the field of cultural heritage conservation by helping researchers build 3D models in computer [18]. OCT is a non-invasive imaging technique that acquires depth-resolved signals with micrometer resolution. OCT is highly advantageous in studying the surface features and subsurface structures of delicate cultural heritage objects such as historical oil paintings and murals. In this field, OCT technology has been applied to

capture high-density (HD) cross-sectional information of paintings to reveal the layer structure [19][20], which is used to examine varnish layer, structural analysis and varnish thickness [21][22]. There are also some other applications such as identifying layer structure of ancient murals and non-invasive [23][24] and monitoring the varnish removal from easel paintings [25] [26][27].

Despite these advantages, the small field-of-view (FOV) of OCT imaging severely limits its potential to cover a mesoscale or macroscopic region of interest (ROI) on a painting. It is difficulty to address the need for both microscopic and macroscopic examinations [28][29]. In our previous study on OCT scanning of oil paintings, we presented a scanning system which performed raster scanning with a pair of galvanometers and extended the range of the lateral FOV by translating the sample painting using a pair linear motor. The larger FOV image is then obtained by stitching imagines obtained with computer technology. However, galvanometers generally have higher resolution and accuracy than linear motors. As a result, the linear motors' translation error can be easily accumulated through each step and leads to overlapping areas in the final stitched image [30].

In this thesis, to solve the above-mentioned problems and better apply the OCT technology in art conservation, we describe a hybrid scanning platform combined with effective algorithm for real-time sampling artifact removal to achieve macroscopic OCT (macro-OCT) imaging which will better assist researchers to investigate the macro/micro structure and construction strategy more directly. The system enables large FOV, HD examination and cross-sectional imaging of oil paintings. Data obtained from the imaging platform can be used to generate the 3D digital copies for the artwork.

CHAPTER 2

OCT THEORY

2.1 Overview

Tomography technique indicates the cross-section imaging capability from a three-dimensional object. Optical coherence tomography (OCT) is a non-invasive method that can acquire the cross-sectional images of the sample with microscopic resolution. OCT is based on low coherence interferometry and can be used to observe the objects with subsurface structural features, particularly for examination of biological tissues. With decades of development, OCT technology has been improved significantly in resolution, sensitivity and imaging speed.

2.2 History of OCT

OCT technology is based on optical coherence-domain reflectometry (OCDR). It started from 1D OCDR and then became a 2D ranging technique. OCDR was applied to check the faults of the optical fiber during manufacture, while OCT was initially used to detect ocular tissues and then applied to other tissues. OCT technology is similar to ultrasound imaging. It measures the echo of light as it travels into the tissue.

Ultrasound biomicroscope (UBM) satisfies this can image the anterior segment with high resolution by using higher frequency sound waves. However, due to the rapid attenuation of high-frequency sound waves in biological tissues, the depth of its detection in the eye is limited. In 1987, Takada et al. developed the optical low coherence interferometry, which turned into a high-resolution optical measurement method with the

support of fiber optics and photoelectric components; Youngquist et al. developed the optical coherence reflectometer, whose light source is a super led directly coupled with optical fiber, one arm containing a reference mirror is located inside the instrument while the optical fiber in the other arm is connected to a device like a camera. All of these laid a theoretical and technical basis for the emergence of OCT.

In 1991, Dr. Huang et al. form MIT declared the technology named Optical Coherence Tomography (OCT). After that, OCT technology was rapidly developed for applications in diagnostic ophthalmology, and other biomedical and nonbiomedical fields.

Courtesy R. Nick Graf
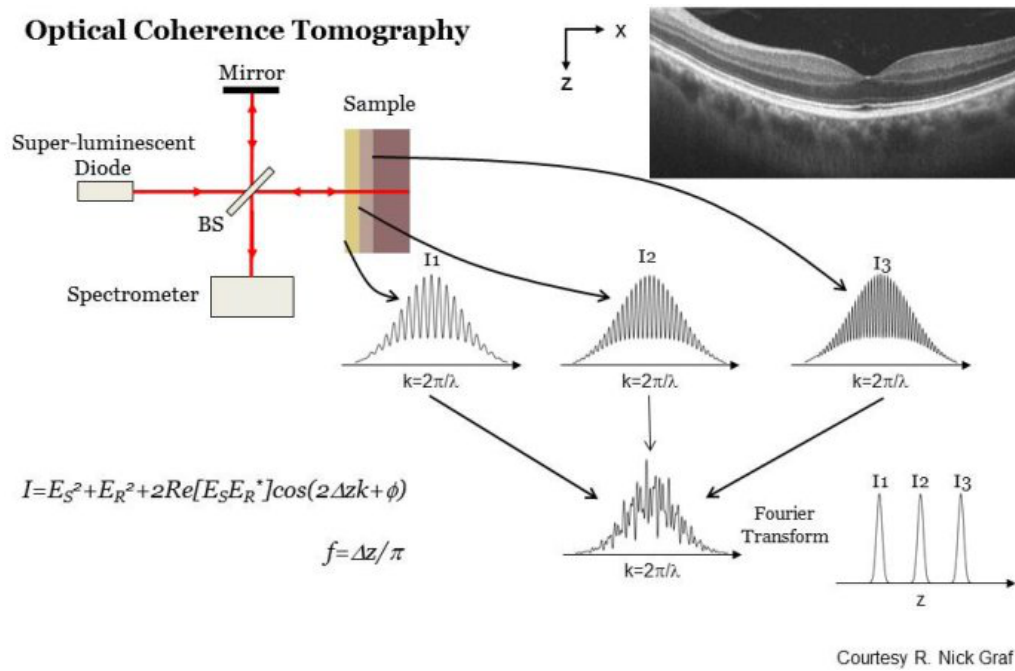
Figure 2.1 OCT developed by Dr. Huang used to measure Retina and coronary artery.

Source: [33].

2.3 Application of OCT

The most important application of OCT technology is in medicine and biology fields. As mention in last section, when the early stage of OCT technology was developed, Dr. Huang

and other scientists used OCT to measure and image the retina, cornea, anterior chamber and iris of human eyes *in vitro* and *in vivo*. After several years of development, OCT system had been further improved and developed into a clinical tool for medicinal workers. OCT was made into a commercial instrument, and finally determined its advantages in fundus and retina imaging. OCT was officially used in ophthalmology in 1995.

OCT as a new optical diagnostic technique is widely used in the area of non-contact and non-invasive tomographic imaging of the micro-structure of the living eye tissue. OCT is an optical analog of ultrasound. Its unique advantage is that its axial resolution depends on the coherence characteristics of the light source and can be higher than $10\mu m$. For ocular imaging, OCT provides sufficient penetration depth because ocular tissues are transparent or semitransparent. OCT can both detect the anterior segment and posterior segment of the eye, and show the morphological structures. It has been widely used in the diagnosis, follow-up observation and effects evaluation of intraocular diseases, especially retinal diseases.
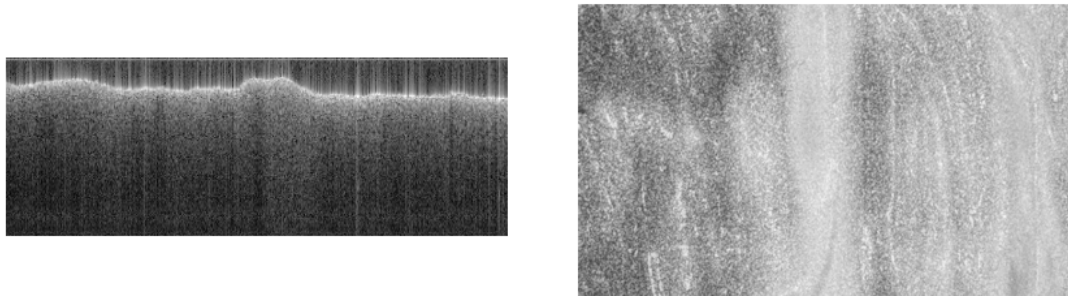
Figure 2.2 OCT B-scan image (left) and *en-face* image based on B-scan (right).

Another important application of OCT in medicinal area is to test the early canceration of soft tissue. The early diagnosis of cancer is essential to save or extend the life of the patient. Currently, the diagnostic gold standard is through biopsy and histology

examination. However, the process is time consuming. and the diagnosis is subjective, limited by the experience of the clinician. It is also difficult to accurately identify the margin of the cancerous area. OCT provides tissue characterization to reveal difference between cancerous tissues and healthy tissues. Therefore, OCT allows real-time tissue characterization and can lead to accurate, and objective diagnosis with computer analysis of OCT signal. As illustrated in Figure 2.3, in the left part of the image, the tissue looks porous and there is a clear border between two types of tissues.
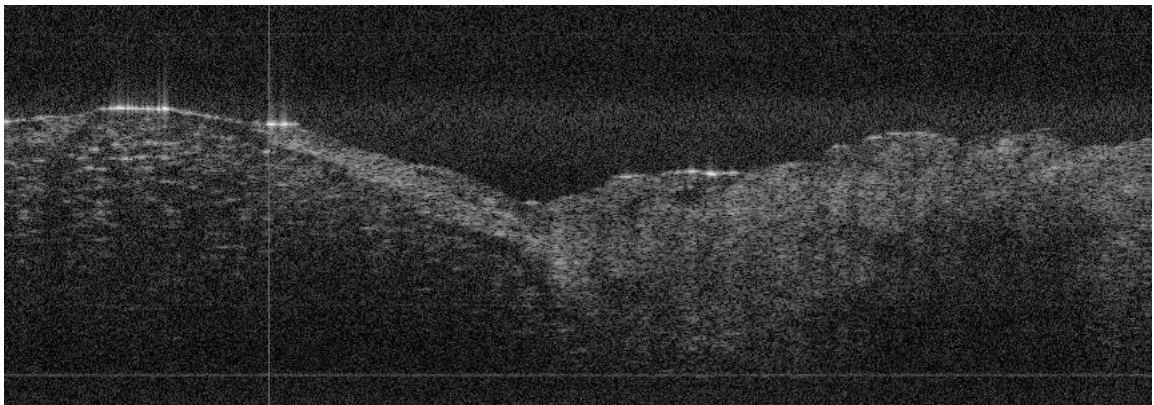
Figure 2.3 OCT B-scan of human breast tissue (left: adipose tissue; right: diseased tissue).

OCT continues to be applied to other medical fields, while OCT technology is also getting into other fields, especially in the field of industrial measurement, such as displacement sensor, thickness measurement of thin film, and non-destructive detection of substructure, high-density data storage. OCT is also used to measure the residual porosity, fiber structure and structural integrity of high scattering polymer molecules. OCT technology can also be used in materials science. M. Bashkansky et al. used the OCT system to test ceramic materials, expanding the application of OCT technology. J.P. Dunkers and other researchers used OCT technology to detect the composite materials without damage [34][35].

2.4 Low Coherence Interferometry

The interferometer is one of the key components in an OCT microscope. This device splits the output of a broadband source into two beams entering reference arm and sample arm E_s. The light incident into the sample arm is focused to a point and scanned. E_r After backscattered by the tissue, the sample light (field E_s) interferes with the reference light (field E_r) and the interference signal is detected. If we assume that the signal detected by the photodetector can be expressed as:

$$I_d = \langle |E_d|^2 \rangle = 0.5(I_r + I'_s) + Re\{\langle E^*_r(t + \tau)E'_s(t)\rangle\} \tag{2.1}$$

, where I_r and I_s represent average intensities from the reference and sample arms of the interferometer. The second term in this equation depends on the optical time delay τ and is determined by the spatial location where the signal originates. It encodes the amplitude of the interference fringes that contain the information about the tissue structure. The property of the interference fringes and wherever the fringes form is all decided by the temporal and spatial coherence characteristics of E'_s and E_r. Therefore, the interferometer has the same function as a cross correlator. It provides a measure of the cross-correlation amplitude. Various techniques have been applied to modulate τ to realize the separation of the cross-correlation signal from the dc component of the intensity.

2.5 Different Mechanisms of OCT

With decades of development, different types of OCT systems have been developed. For the time domain OCT system, the detection of different depths is realized by the fast scanning the optical path length of the reference arm (Figure 2.4).
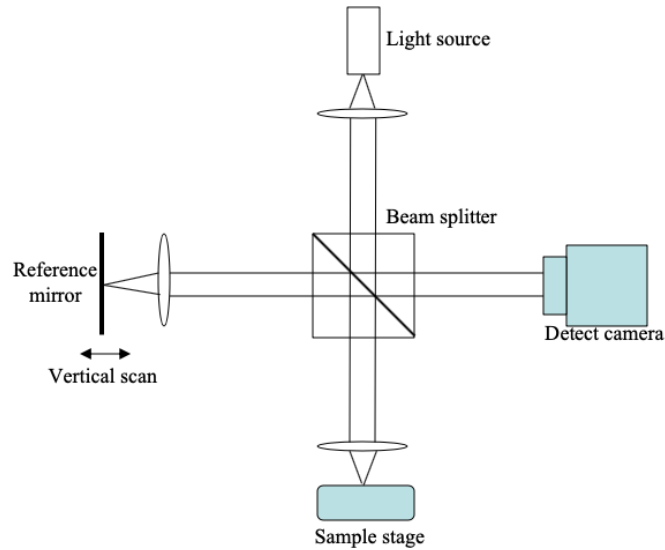
Figure 2.4 Time-domain OCT system diagram.

In a frequency-domain OCT system, the spectrum of the interference signal is detected. Afterwards, depth resolved sample profile is obtained by fast Fourier inverse transform on the interferometric spectrum. In frequency-domain OCT, the reference arm is fixed and does not perform mechanical optical path scanning. The interference signal is the coherent superposition of the scattered light from different depths of the sample and the reference light. The theory of FD-OCT is equivalent to that of the inverse process of Fourier spectrometer. The spectral width determines the longitudinal depth resolution. The spectral resolution determines the maximum depth of the scattered signal.
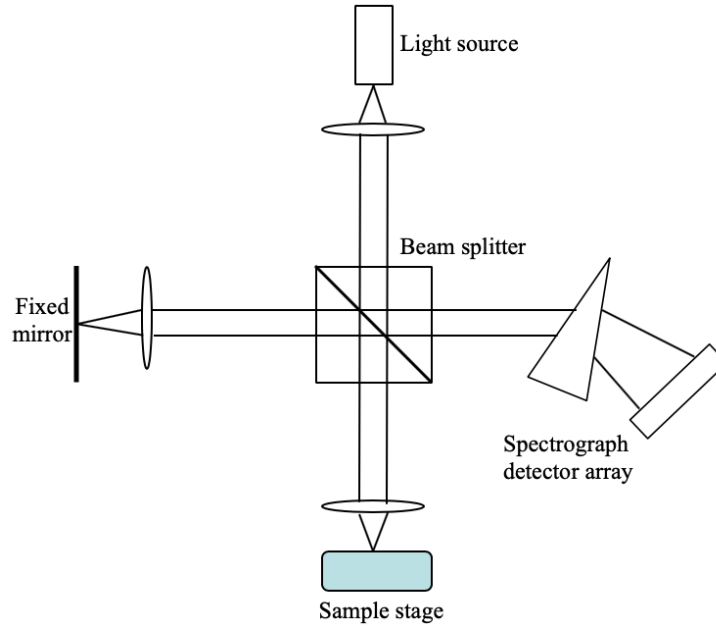
Figure 2.5 Frequency-domain OCT system diagram.

The advantage of frequency domain OCT is that it does not need the longitudinal scanning of the reference arm and its signal-to-noise ratio is not directly related to the bandwidth of the light source. As a result, there is no tradeoff between the signal-to-noise ratio and the longitudinal resolution. Experimental results showed that frequency domain OCT had a 20dB to 30dB advantage in sensitivity compared to time domain OCT and the sensitivity of frequency domain OCT can be higher than 100dB.

CHAPTER 3

CORRELATION COEFFICIENT

3.1 Introduction

Three kinds of correlation coefficients are frequently used in Statistics: Pearson correlation coefficient, Spearman correlation coefficient and Kendall correlation coefficient.

Pearson correlation coefficient reflects the degree of linear correlation [31]. Consider two variables: X and Y.

(1) If X and Y have no correlation, the correlation coefficient is 0,

(2) The two variables X, Y are positively correlated (the correlation coefficient is between 0.00 and 1.00), if the value of X increases or decreases while the value of Y increases or decreases.

(3) The two variables X, Y are negatively correlated (the correlation coefficient is between - 1.00 and 0.00), if the value of X increases or decreases while the value of Y decreases or increases.

When the absolute value of the coefficient is closed to 1, the two variables have high correlation. On the other hand, if the coefficient is closed to 0, the two variables have low correlation.

3.2 Pearson Correlation Coefficient

Pearson correlation coefficient is also called as Pearson product moment correlation coefficient and is a linear correlation coefficient. Pearson correlation coefficient is a statistic reflection of the linear correlation degree between two variables.

Pearson correlation coefficient between two variables is defined as the quotient of covariance and standard deviation between two variables:

$$\rho_{x,y} = \frac{cov(x,y)}{\sigma_x \sigma_y} \tag{3.1}$$

$$\rho = \frac{\sum_{i=1}^{N}(x_i - \bar{x})(y_i - \bar{y})}{\sqrt{\sum_{i=1}^{N}(x_i - \bar{x})^2 \sum_{i=1}^{N}(y_i - \bar{y})^2}} \tag{3.2}$$

The Pearson correlation coefficient ($\rho_{x,y}$) of two continuous variables (x, y) is equal to the covariance $cov(x, y)$ between them divided by the product of their respective standard deviations (σ_x, σ_y). The value of coefficient is always between - 1.0 and 1.0. As discussed previously, variables with Pearson correlation coefficient close to 0 are called uncorrelated, and variables with Pearson correlation coefficient close to 1 or - 1 are called strongly correlated.

When this correlation coefficient is used to determine the relationship between the two variables, there are some limitations [32]. Data involved in Pearson correlation calculation should be drawn from normal distributions. The statistical difference between X and Y cannot be too large. Otherwise, the Pearson correlation coefficient is largely affected by outliers.

3.3 Spearman Correlation Coefficient

Spearman correlation coefficient, also names rank correlation coefficient, is a nonparametric statistical method. The calculation of Spearman correlation coefficient uses the rank position of two variables for linear correlation analysis. It does not require knowing the distribution of the variables involved in correlation calculation. Spearman

correlation coefficient is more widely used than Pearson coefficient. However, it requires more computation. Spearman rank correlation is a method that studies the correlation between two variables based on ranked data. It is calculated according to the difference between the two pairs of grades. Hence, it is also called 'grade difference method'.

As long as the observation values of two variables are paired grade evaluation data, or grade data obtained from continuous variable observation data, regardless of the overall distribution form and sample capacity of the two variables, the correlation analysis can be conducted by using the Spearman grade correlation.

For the data subject to Pearson correlation coefficient, Spearman correlation coefficient can also be calculated, but at a lower speed.

3.4 The Application of Correlation Coefficient in Image Stitching

The correlation coefficient is often used to quantify the correlation of two sets of data. Images are stored as matrixes in computer. Two images with overlapping area can be stitched into one picture with a larger field of view. As shown in Figure 3.1, two images (enface OCT images) have an overlapping region. Once the overlapping parts are found, these two images can be stitched together seamlessly. The pixels in red box can be considered as two matrices sets with the same size. By calculation the Pearson or Spearman coefficient, the correlation degree can be determined. As mentioned before in above sections, the best match of these two matrices is when the correlation coefficient is approximately 1. Hence by identifying the peak of the correlation coefficient will allow one to find the overlapping region and stitch two images to extend the field of view.
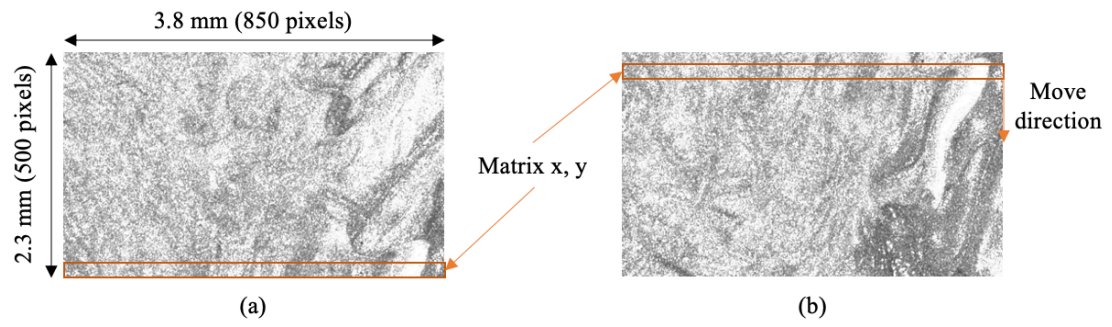
Figure 3.1 *en-face* original OCT images.

CHAPTER 4

SYSTEM CONFIGURATION AND IMAGE PROCESSING

4.1 System Components

The macro-OCT imaging system is shown in Figure 4.1. In this study, we use a swept source OCT (SS OCT) system for 3D imaging. The SS-OCT system (Axsun) works at 1.06μm with 100nm bandwidth, 100 kHz Ascan rate. The build-in fiber-optic Michelson interferometer is illuminated by the swept source. A lens is fixed at the sample arm (Thorlabs LSM04-BB) to focus the probing beam and collect photons backscattered from the surface or the subsurface layers of the sample. The photon detector is used to detect the interferometric signal. A frame grabber (PCIe-1433, National Instrument) is used to acquire the data and stream the data. To augment the capability of the computer in processing image data, a GPU (NVIDIA gtx1080) for parallel signal processing.

The hybrid scanning system consists of two major scanning modules to acquire data from a large field of view. The first module is the galvo system with two galvanometers (Thorlabs GVS002) steering the incident light beam in x and y directions for lateral scanning. The lateral range of galvo scanning is determined by the voltage applied. FOV_x and FOV_y are directly decided by several factors: the focal length of the imaging objective (F_{obj}=54mm), the responsive factor of the galvanometer deflection angle to voltage, and the voltage applied to the galvanometer (V_x and V_y): $FOV_x=2\beta V_x F_{obj}$ and $FOV_y=2\beta V_y F_{obj}$.

The second module of scanning is a pair of linear motors with long translation range to increase the FOV of OCT imaging by exposing different parts of the sample to the object lens without compromising spatial resolution. The model of XYZ linear motor stage is

Intellidrives (Intellidrives X1-BEMA-W45-600) assembled by our collaborators. The control of X and Y stages is integrated into the OCT imaging system (receives signal from the Arduino chip microcomputer). The translation resolution of the X and Y stages is 18.75 μm. As presented in Figure 4.1, a workstation computer (Dell Precision 5530) is used to coordinate and synchronize different modules of the macro-OCT system. The C++ program that synchronizes the data acquisition card (DAQ, National Instruments NI 6212) with galvo scanning is developed in-house. To establish the connection between the workstation and the motor system, the in-house developed software synchronizes the XY motion of the linear stage by sending sync signal to the MCU (Arduino UNO REV3) using a data acquisition device (DAQ). Once the whole system is synchronized, the OCT images captured during each step is saved and processed. The imaging depth of OCT is about 2.5 mm. This depth allows us to obtain the 3D topology of the sample surface and subsurface part. The size of the 3D data cute is quite large (about 250 MB). To generate an image with macroscopic FOV, tens of 3D data cubes are acquired. It is challenging to manage such a huge volume of data and perform image stitching. To address this issue, we convert volumetric OCT data sets (3D) into 2D matrices, and perform analysis to stitch the data using the 2D matrices. We average the 3D data along the axial (z) dimension to get an *en-face* image of the sample. This effectively converts 3D data to 2D while preserves information needed for image stitching.
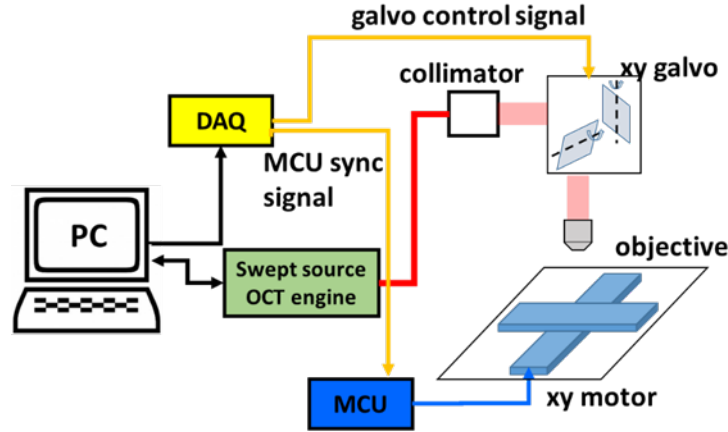
Figure 4.1 The configuration of macro-OCT based on a hybrid scanning platform.

4.2 Lateral Scanning and Data Acquisition Protocol for Macro-OCT Imaging

Lateral scanning motion path for the macro-OCT imaging is shown in Figure 4.2. First, the macro-OCT system performs data acquisition from the sample at lateral coordinate (x_1, y_1). The galvo in the system will be driven by the signal from the workstation computer and steer the laser beam to perform area scanning. The image acquisition system obtains volumetric OCT data from an area represented by the rectangle shaded in blue, marked as ROI_1. ROI_1 centers at (x_1, y_1) with x dimension of FOV_x and y dimension of FOV_y. After the OCT system finishes data acquisition in ROI_1, the linear motors will receive the command from the MCU (triggered by program in computer). Once received the command, the MCU drives the motor in x dimension and/or in y dimension to move to a new lateral coordinate (x_2, y_2). At the same time, the image acquisition stops, and unit next command arrives. After the linear stage travels to the desired spatial coordinate, the OCT engine resumes volumetric data acquisition in the new area (ROI_2) centered at (x_2, y_2). This is again followed by linear motor translation. The process of data acquisition and motor translation repeats for N times. N sets of volumetric OCT data are obtained at (x_1, y_1), $(x_2,$

y_2), (x_3, y_3), …, and (x_N, y_N). For Figure 4.2, N = n*p, where n is 10, and p is 9. These lateral coordinates are predefined, and the scanning pathway is presented in Figure 4.2.
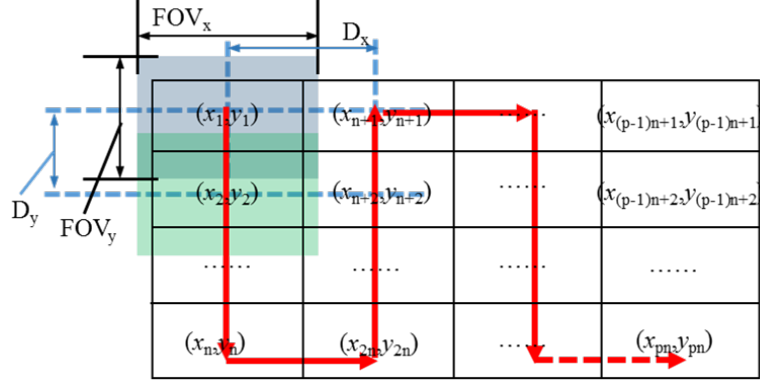
Figure 4.2 Lateral scanning for macro-OCT imaging.

4.3 Image Stitching Methods

The scanning strategy scans ROIs with lateral overlap. This ensures that every point on the lateral plane of the sample is scanned for OCT imaging. If the step size of the linear motor is precisely FOV_x or FOV_y, some areas between two adjacent ROIs may be missing, because the translation accuracy of the linear motor is limited. As shown in Figure 4.2, we set the size $D_x < FOV_x$ and $D_y < FOV_y$. D_x and D_y are the translation step sizes in the X and Y direction for the linear stage. Such a redundant scanning strategy is applied to prevent the problem mentioned above because the accuracy of the galvanometers and the linear motor are not at the same level (1.5μm scanning resolution for galvanometers and 18.75μm for motors). The overlapping width is set to 300 μm due to the step size of the motor. To generate an image without redundancy artifact, we need to remove the redundant parts in each image and stitch all the images together. The overlapping areas between two adjacent images are not always with the same size, because of the inaccuracy in linear motor translation. In order to obtain the high quality artifact-free OCT image with large FOV, we

introduce the method based on cross-correlation analysis to adaptively stitch S_0, S_1, …, and S_{N-1}, where $S_k \in R^{N_x \times N_y \times N_z}$ are volumetric OCT data sets obtained with the sample located at (x_k, y_k).

Consider the imaging system acquires two adjacent volumetric OCT data sets denoted as S_k and S_{k+1}. To digitally align the acquired data, we first translate 3D data sets S_k and S_{k+1} to 2D by the method described above. The resultant data sets are presented as M_k and M_{k+1} ($M_k \in R^{N_x \times N_y}$ and $M_{k+1} \in R^{N_x \times N_y}$), as shown in Figure 4.3 (a) and (b). When S_k and S_{k+1} are directly stitched together as shown in Figure 4.3 (c), the same region (areas enclosed by the dashed rectangular boxes) will appear twice as image artifact. To remove artifacts due to redundant OCT scanning, we select a submatrix from the bottom of M_k, written as m_k that contains a few numbers of rows (usually 5 rows in our algorithm,). In the second image (M_{k+1}), we select the matrix at top of the image, and determine a submatrix within M_{k+1} that best matches m_k which is marked as m_{k+1} that contains h rows of data from M_{k+1} (Figure 4.3 (b)). We calculate the Pearson correlation coefficient between m_k and m_{k+1} using Eq (4.1). In this equation, $E(\ )$ represents the expectation value, • represents element-wise product, and σ_v represents the standard deviation of v. According to the principle described in chapter 3, when ρ is closer to 1, m_k and m_{k+1} are extremely similar. We use a window sliding along y direction pixel by pixel to select m_{k+1} that consists of wth to $(w+h-1)^{th}$ row of M_{k+1}, calculate a set of ρ, and determine the w that corresponds to the largest ρ. If the biggest ρ appears and is also closed to 1 (if ρ is far away from 1, the result may not be used), we will attach data of M_{k+1} to M_k, starting from wth Bscan, stitching into an artifact free image (Figure 4.3 (d)). The same data stitching strategy applies to every set of OCT data.

$$\rho = \frac{E[(m_k - \bar{m}_k) \cdot (m_{k+1} - \bar{m}_{k+1})]}{\sigma_{m_k} \sigma_{m_{k+1}}} \tag{4.1}$$

After data stitching in y direction, a similar approach is utilized to stitch images in x direction.
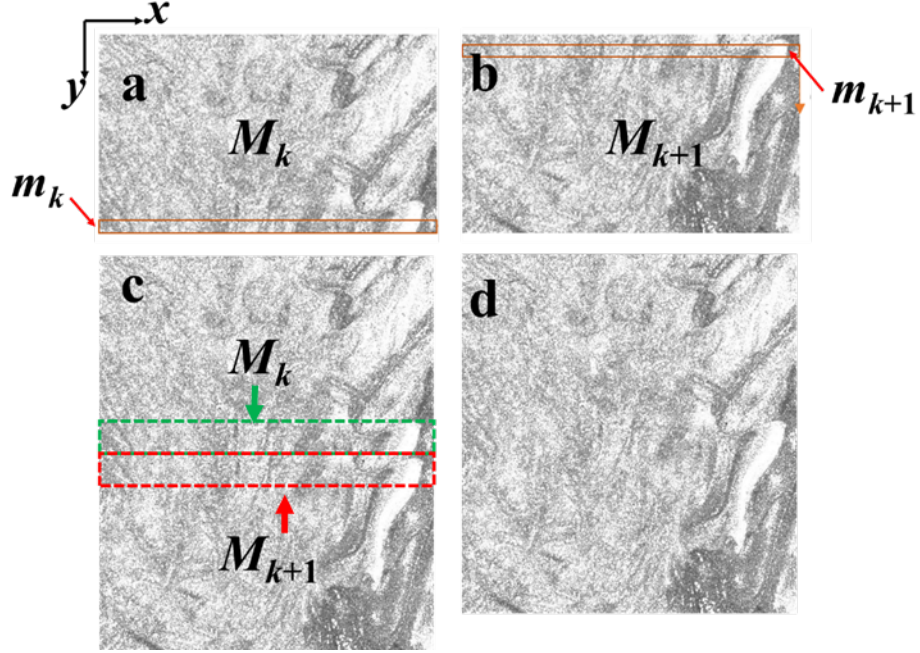

Figure 4.3 Illustration of image stitching strategy (a) An *enface* OCT image of the oil painting; (b) An *enface* OCT image of the oil painting with the sample translated in y direction; (c) Images directly stitched together with redundant artifact; (d) Images stitched together through cross-correlation analysis after redundant artifact removal.

CHAPTER 5

RESULTS

In this experiment, we described a macro-OCT imaging study based on the oil painting produced by an artist that mimics the impressionist style. The size of the canvas painting is of 10 cm by 10 cm, shown in Figure 5.1. This painting style is suitable to our project because of its unique brushstrokes and style to demonstrate the 3D reconstruction capability of the optical imaging system.
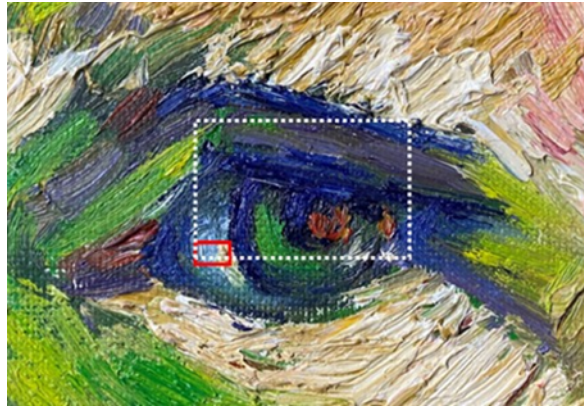
Figure 5.1 The photo of sample painting.

Without the hybrid scanning platform, an OCT system acquires volumetric data from a region denoted by the red box in Figure 5.1. The Ascan, Bscan, enface image and 3D rendered volume of this area is shown in Figure 5.2 (a) – (d). The Ascan obtained from oil painting (Figure 5.2 (a)) indicates the depth penetration of the OCT signal. The Bscan (Figure 5.2 (b)) shows clear visible speckle pattern due to the high-density OCT imaging. In addition, it shows the variation of surface profile. The enface image in Figure 5.2 (c) was obtained by averaging pixel values along axial dimension z. Figure 5.2 (d) demonstrates the rendered surface topography of the paint in this area (solid red box in Figure 5.1).
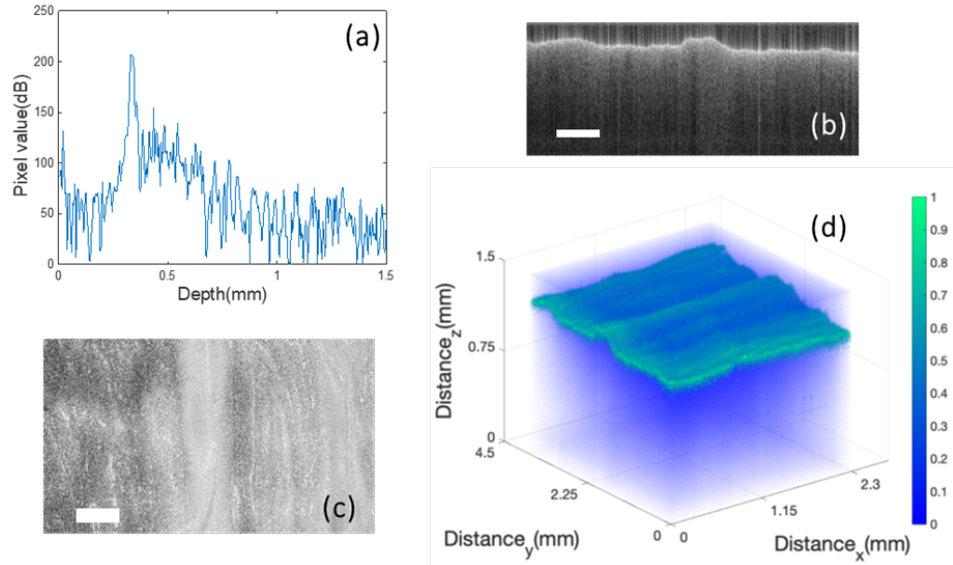
Figure 5.2 (a) Ascan (b) Bscan OCT image; (c) Enface image; (d) 3D rendered volume. In (b) and (c), scale bar = 0.5 mm.

We further demonstrated the macro-OCT's capability for large FOV, HD OCT imaging to reconstruct the 3D surface profile of the painting. The sample was translated by the motor system to different lateral positions following data acquisition protocol shown in Figure 3.2 (n=10 and p=9). OCT images were acquired at 90 transverse coordinates. A 27mm by 18mm range of FOV was achieved by scanning the ROIs (dotted line in Figure 4.2). The Pearson and Spearman correlation coefficient methods as we mentioned in chapter 3 are used to stitch the images. The stitched *en-face* image obtained by averaging OCT data along axial dimension z is shown Figure 5.2 (a) with the 5mm scale bar. We performed peak detection for each Ascan to identify the surface location in axial dimension to create the 3D characteristics information for the area we got as Figure 5.2 (a) shows. Figure 5.2 (b) represents the surface topography information in grey scale with white part presenting high altitude and black for the lower place.
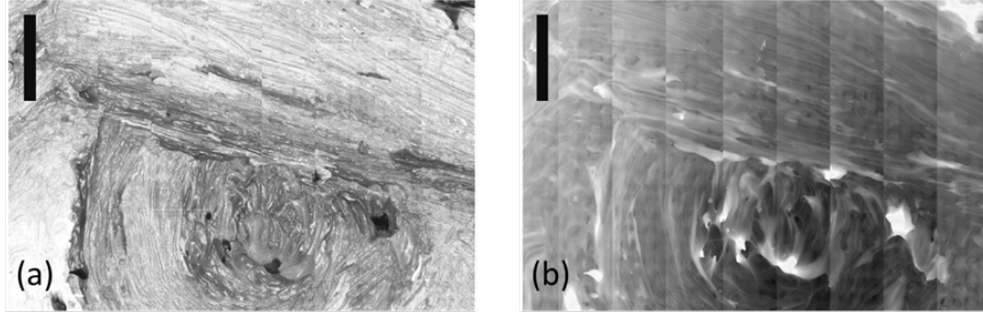
Figure 5.3 (a) Stitched enface image of the ROI; (b) Stitched surface topography of ROI. Scale bar = 5 mm.

We found the best match and combine the color photo and the surface topography model information with 3D plug-in software (3D map generator) from Adobe Photoshop. Frist, according to the grayscale height image shown as Figure 5.3 (b), the program generated a 3D black-and-white topography model, and then we captured the colorful 2D spectral image of the ROI. The software generated the 3D spectral reconstruction of the ROI by overlapping the 2D spectral image and the 3D topography model in one direction. The final production contained both spectral and texture information. Figure 5.4 presents the spectral 3D reconstruction of the ROI on the painting (white dotted area in Figure 5.1).
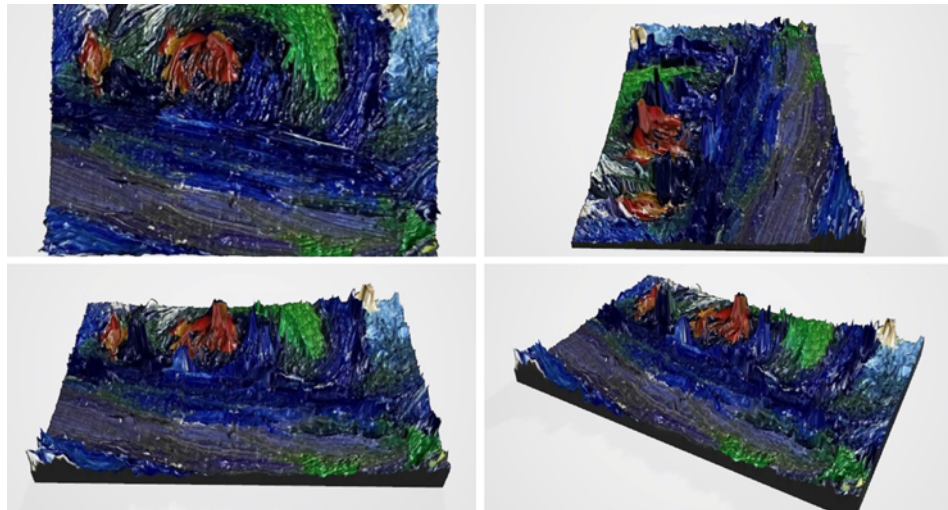
Figure 5.4 Spectral and texture of the ROI from the impressionist oil painting.

With the digital 3D model, combined with the 3D print technology, we generated a

3D printed copy of the oil painting (Figure 5.5).
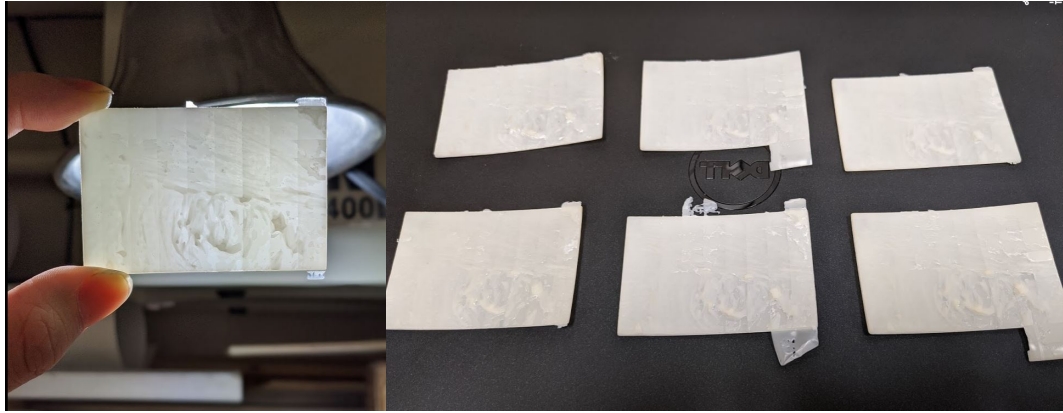
Figure 5.5 Reproduced oil painting 3D models.

CHAPTER 6

CONCLUSION

In conclusion, this thesis describes a macroscopic OCT imaging system with hybrid scanning platform. The imaging system allows spectral 3D reconstruction of precious art works and potentially other cultural heritage objects. Using a novel image stitching technology, the image system performs high-resolution, high-density OCT imaging with macro-view. The digital copy generated by OCT scanning can be a backup to preserve invaluable artworks with great detail, as war, terrorism, natural disaster, and other catastrophes may put art works in a vulnerable position.

REFERENCES

[1] Fernandes, Pedro. "Applied microbiology and biotechnology in the conservation of stone cultural heritage materials." *Applied microbiology and biotechnology* 73.2 (2006): 291.

[2] Carlomagno, Giovanni Maria, et al. "Infrared thermography and geophysical techniques in cultural heritage conservation." *Quantitative InfraRed Thermography Journal* 2.1 (2005): 5-24.

[3] Schmitt, Joseph M. "Optical coherence tomography (OCT): a review." *IEEE Journal of selected topics in quantum electronics* 5.4 (1999): 1205-1215.

[4] Hassan, Taimur, et al. "Review of OCT and fundus images for detection of Macular Edema." *2015 IEEE International Conference on Imaging Systems and Techniques (IST)*. IEEE, 2015.

[5] Welzel, Julia. "Optical coherence tomography in dermatology: a review." *Skin Research and Technology: Review article* 7.1 (2001): 1-9.

[6] N. Yastikli, "Documentation of cultural heritage using digital photogrammetry and laser scanning," *J. Cult. Herit.*, vol. 8, no. 4, pp. 423–427, 2007.

[7] N. Gaburro, G. Marchioro, and C. Daffara, "A versatile optical profilometer based on conoscopic holography sensors for acquisition of specular and diffusive surfaces in artworks," in *Optics for Arts, Architecture, and Archaeology VI*, 2017, vol. 10331, no. July 2017, pp. 48–56.

[8] G. Y. Sirat, "Conoscopic holography. I. Basic principles and physical basis," *J. Opt. Soc. Am. A*, vol. 9, no. 1, pp. 70–83, Jan. 1992.

[9] I. Alvarez, J. M. Enguita, M. Frade, J. Marina, and G. Ojea, "On-line metrology with conoscopic holography: beyond triangulation," *Sensors (Basel).*, vol. 9, no. 9, pp. 7021–7037, 2009.

[10] a Della Patria *et al.*, "Index 2D IMAGING AND 3D SENSING DATA ACQUISITION AND REGISTRATION FOR PAINTING CONSERVATION 2D IMAGING AND 3D SENSING DATA ACQUISITION," vol. 5665, pp. 1–12, 2005.

[11] R. Fontana *et al.*, "Integrating 2D and 3D data for diagnostics of panel paintings," in *Optical Metrology for Arts and Multimedia*, 2003, vol. 5146, pp. 88–98.

[12] G. Guidi, C. Atzeni, and S. Lazzari, "3D optical scanning diagnostics for Leonardo Da Vinci's," in *3-D Digital Imaging and Modeling, 2003. 3DIM 2003. Proceedings. Fourth International Conference on*, 2003, pp. 110–115.

[13] M. L. Story, F. Blais, L. Cournoyer, J. Beraldin, and M. Picard, "3D Imaging from Theory to Practice : The 3D imaging from theory to practice : the Mona Lisa story," *Opt. Eng.*, vol. 7060, pp. 1–10, 2008.

[14] J. Dong, A. Locquet, M. Melis, and D. S. Citrin, "Global mapping of stratigraphy of an old-master painting using sparsity-based terahertz reflectometry /639/624/400/561 /639/624/1107/510 /123 article," *Sci. Rep.*, vol. 7, no. 1, pp. 1–12, 2017.

[15] C. L. Koch Dandolo *et al.*, "Toward a multimodal fusion of layered cultural object images: complementarity of optical coherence tomography and terahertz time-domain imaging in the heritage field," *Appl. Opt.*, vol. 58, no. 5, p. 1281, 2019.

[16] M. Schreiner, B. Frühmann, D. Jembrih-Simbürger, and R. Linke, "X-rays in art and archaeology: An overview," *Powder Diffr.*, vol. 19, no. 01, pp. 3–11, 2004.

[17] D. N. H. Notman *et al.*, "Modern imaging and endoscopic biopsy techniques in Egyptian mummies," *Am. J. Roentgenol.*, vol. 146, no. 1, pp. 93–96, Jan. 1986.

[18] C. S. Cheung, J. M. O. Daniel, M. Tokurakawa, W. A. Clarkson, and H. Liang, "High resolution Fourier domain optical coherence tomography in the 2 μm wavelength range using a broadband supercontinuum source," *Opt. Express*, vol. 23, no. 3, pp. 1992–2001, Feb. 2015.

[19] M. W. A. K. Piotr Targowski Bogumiła Rouba, P. Targowski, B. Rouba, M. Wojtkowski, and A. Kowalczyk, "The Application of Optical Coherence Tomography to Non-Destructive Examination of Museum Objects," *Stud. Conserv.*, vol. 49, no. 2, pp. 107–114, 2004.

[20] P. Targowski and M. Iwanicka, "Optical coherence tomography: Its role in the non-invasive structural examination and conservation of cultural heritage objects-A review," *Appl. Phys. A Mater. Sci. Process.*, vol. 106, no. 2, pp. 265–277, 2012.

[21] P. Targowski, M. Iwanicka, M. Sylwestrzak, C. Frosinini, J. Striova, and R. Fontana, "Using Optical Coherence Tomography to Reveal the Hidden History of The Landsdowne Virgin of the Yarnwinder by Leonardo da Vinci and Studio," *Angew. Chemie - Int. Ed.*, vol. 57, no. 25, pp. 7396–7400, 2018.

[22] H. Liang *et al.*, "En-face optical coherence tomography - a novel application of non-invasive imaging to art conservation.," *Opt. Express*, vol. 13, no. 16, pp. 6133–6144, 2005.

[23] P. Targowski, M. Góra, and M. Wojtkowski, "Optical Coherence Tomography for Artwork Diagnostics," *Laser Chem.*, vol. 2006, pp. 1–11, 2006.

[24] T. Arecchi *et al.*, "A new tool for painting diagnostics: Optical coherence

tomography," *Opt. Spectrosc.*, vol. 101, no. 1, pp. 23–26, 2006.

[25] I. Gorczynska *et al.*, "Varnish Thickness Determination by Spectral Optical Coherence Tomography," *Lasers Conserv. Artworks*, pp. 493–497, 2007.

[26] H. Liang, R. Lange, H. Howard, and J. Spooner, "Non-invasive investigations of a wall painting using optical coherence tomography and hyperspectral imaging," *Proc. SPIE*, vol. 8084. pp. 80840F-80840F–7, 2011.

[27] M. Iwanicka *et al.*, "Complementary use of Optical Coherence Tomography (OCT) and Reflection FTIR spectroscopy for in-situ non-invasive monitoring of varnish removal from easel paintings," *Microchem. J.*, vol. 138, pp. 7–18, 2018.

[28] S. Song, J. Xu, and R. K. Wang, "Long-range and wide field of view optical coherence tomography for in vivo 3D imaging of large volume object based on akinetic programmable swept source," *Biomed. Opt. Express*, vol. 7, no. 11, p. 4734, 2016.

[29] F. Zaki, I. Hou, D. Cooper, D. Patel, Y. Yang, and X. Liu, "High-definition optical coherence tomography imaging for noninvasive examination of heritage works," *Appl. Opt.*, vol. 55, no. 36, p. 10313, Dec. 2016.

[30] X. Liu, Y. Huang, and J. U. Kang, "Distortion-free freehand-scanning OCT implemented with real-time scanning speed variance correction," *Opt. Express*, vol. 20, no. 15, pp. 16567–16583, Jul. 2012.

[31] Benesty, Jacob, et al. "Pearson correlation coefficient." *Noise reduction in speech processing*. Springer, Berlin, Heidelberg, 2009. 1-4.

[32] Havlicek, Larry L., and Nancy L. Peterson. "Robustness of the Pearson correlation against violations of assumptions." Perceptual and Motor Skills 43.3_suppl (1976): 1319-1334.

[33] D. Huang, E. A. Swanson, C. P. Lin, J. S. Schuman, W. G. Stinson, W. Chang, M. R. Hee, T. Flotte, K. Gregory, and C. A. Puliafito, "Optical coherence tomography," Science, vol. 254, no. 5035, pp. 1178–1181, 1991.

[34] Bashkansky, Mark, and John F. Reintjes. "Method and apparatus for reducing speckle in optical coherence tomography images." U.S. Patent No. 6,847,449. 25 Jan. 2005.

[35] Dunkers, Joy P., et al. "Optical coherence tomography of glass reinforced polymer composites." Composites Part A: Applied Science and Manufacturing 30.2 (1999): 139-145.